Bulletin of the Seismological Society of America, Vol. 103, No. 1, pp. 394–411, February 2013, doi: 10.1785/0120110232

Determining Fault Geometry from the Distribution of Coseismic Fault Slip Related to the 2006 Taitung Earthquake, Eastern Taiwan

by Laetitia Mozziconacci, Bertrand Delouis, Bor-Shouh Huang, Jian-Cheng Lee, and Nicole Béthoux

Abstract On 1 April 2006, the Taitung earthquake (M_w 6.1) occurred in Taiwan at the boundary between the Philippine Sea and Eurasian plates, where high convergence rates contributed to the development of Plio-Pleistocene orogeny in the region. From the joint inversion of seismic and geodetic data, we identified the event's fault geometry and reconstructed the distribution of coseismic fault slip. We modeled fault geometries with increasing complexity and selected the model that best reproduced all datasets, simultaneously. Even though the earthquake magnitude was moderate, rupturing occurred in two steps. The initial rupture was generated on a listric, north–south-trending fault (for which dip decreases with increasing depth), and was immediately followed by movement along a perpendicular structure that cross-cuts the main fault at 5 km south of the earthquake hypocenter. The average slip along the rupture was 30 cm, with a maximum of 87 cm. Oblique-reverse fault movement was characterized by a predominant left-lateral component. The amount of slip is well constrained for offsets of more than 5 cm, with an associated uncertainty of 32%. For slip amounts greater than 5 cm, uncertainties on rake and rupture time are 11° and 0.54 s, respectively. The rupture propagated from the hypocenter bilaterally, moving slightly faster toward the south (2.5 ± 0.4 km/s) than to the north (1.7 ± 0.1 km/s). To the south, the rupture was rapidly transmitted upward at the junction with the cross-cutting east–west segment, whereas in the north, the rupture remained confined to the lower segment of the main fault. From Global Positioning Systems (GPS) and seismic data (time window < 1 min), we infer that the cross-cutting segment was activated following coseismic rupture on the main north–south fault, yet close enough in time to be associated with coseismic movement acquired by GPS (daily solutions).

Introduction

Ongoing orogenesis in Taiwan is the result of active collision between the Eurasian plate (EUP) and the Philippine Sea plate (PSP). At the junction of these plates lies the Longitudinal Valley (LV), a narrow valley filled by late Quaternary sediments (Tsai *et al.*, 1974). The LV trends north-northeast–south-southwest, extending over a length of 150 km without exceeding 10 km in width. Previous studies define the LV as the plate suture (Ho, 1986; Tsai, 1986) connecting the Central Range (CER) to the west (part of the EUP) with the Coastal Range (COR; part of the PSP) to the east (Fig. 1, left side). The LV accommodates horizontal shortening at a rate of about 20–30 mm/yr (Yu *et al.*, 1990; Lee and Angelier, 1993; Yu and Kuo, 2001), corresponding to 25%–30% of total plate convergence (Lee *et al.*, 1998; Angelier *et al.*, 2000) that explains the high seismicity of this region. Shortening is accommodated mainly along a structure located on the eastern side of the LV that strikes parallel to the LV and dips to the east: the Longitudinal Valley fault (LVF; Fig. 1, right side). However, Shyu *et al.* (2006, 2008) speculate that some minor shortening occurs along a west-dipping fault on the western side of the valley: the Central Range fault (CRF). The amount of shortening along the CRF is uncertain. The LVF is one of the most active structures in Taiwan, as the major plate boundary fault (Biq, 1972; Chai, 1972; Ho, 1986). Oblique collision between the PSP and the EUP results in oblique movement along the LVF (reverse and left-lateral). Faulting along the CRF has proven difficult to characterize, given the scarcity of surface exposure and a lack of recorded seismic activity. However, on the basis of uplifted fluvial terraces, it has been proposed that the CRF is a feature related to thrusting (Biq, 1965; Shyu *et al.*, 2006).

The Taitung earthquake (M_w 6.1) occurred on 1 April 2006, just west of the southern part of the LV (Central Weather Bureau [CWB], see Data and Resources; Wu *et al.*, 2006), along the eastern flank of the CER (Fig. 1, left side), in the transition area between a mature collision zone to the north

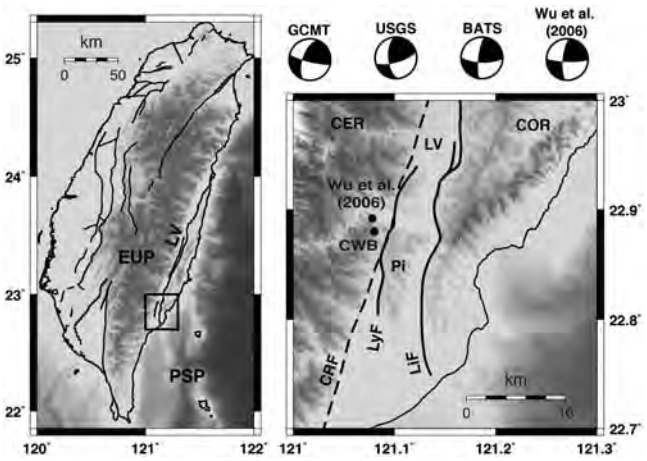

Figure 1. Location of the 2006 Taitung earthquake. (left) A general map of Taiwan showing the Eurasian plate (EUP) and the Philippine Sea plate (PSP) separated by the narrow Longitudinal Valley (LV). Black lines are active faults. (right) Location map of the Taitung earthquake. The epicenter from the Central Weather Bureau (CWB) and the relocated epicenter of Wu *et al.* (2006) lie very close to one another on the eastern border of the Central Range (CER). Active faults are black lines: the Luyeh fault (LyF) and the Lichi fault (LiF) lie along either side of the Peinanshan massif (Pi), within the LV and west of the Coastal Range (COR). The Central Range fault (CRF) is shown to run along the eastern border of the CER and is plotted with a dotted black line. Focal mechanisms corresponding to different networks (referred to as GCMT, USGS, and BATS) or a specific study (Wu *et al.*, 2006) are plotted above the map, indicating a similar strike-slip behavior for this event.

and an oceanic subduction zone to the south. Different seismic networks (Table 1; Fig. 1, right side) give the same strike-slip focal mechanism for the Taitung earthquake with a north–south striking nodal plane that dips steeply to the west, whereas the other plane is oriented east–west and dips almost vertically southward. Because no surface rupture was observed for this event (Chen *et al.*, 2009), a comparison of nodal plane geometries with local geological structures would help to identify the fault plane.

Near the epicenter, the LVF divides into two branches that run along either side of the Peinanshan massif, a hill of conglomerate composed of fluvial deposits with CER-derived clasts (Page and Suppe, 1981; Barrier and Angelier, 1986; Teng *et al.*, 1988). In this area, oblique movement along the LVF is partitioned between the two branches. To the east of the massif, the Lichi fault (or Peinan branch) accommodates mainly strike-slip movement; the reverse component of plate convergence takes place on the Luyeh fault, the western branch (Lee *et al.*, 1998; Shyu *et al.*, 2006, 2008; Peyret *et al.*, 2011). As both faults have the same eastward dip as the main segment of the LVF (e.g., Lee *et al.*, 1998; Shyu *et al.*, 2006, 2008) and the epicenter of the Taitung earthquake is located to the west of those structures, we conclude that neither fault caused the earthquake. Another possible candidate that might account for the north–south nodal plane is the CRF. On the basis of observations of uplifted fluvial terraces, Shyu *et al.* (2006, 2008) inferred that the CRF should exist in the vicinity of the epicenter as a blind, west-dipping fault overlapped by the Luyeh fault. Because the geometry of the CRF and the orientation of the north–south nodal plane are comparable, and the earthquake epicenter is, in this case, located to the west of the CRF, we infer that the earthquake is likely originated by the CRF. However, this interpretation is complicated by the existence of steep strike-slip conjugate faults within the Peinanshan massif (Barrier *et al.*, 1982; Yü, 1996; Lee *et al.*, 1998), with one set oriented at N95°E. This direction is in agreement with the strike of the second Taitung earthquake nodal plane. Consequently, for the Taitung earthquake, the ambiguity between nodal planes is not solved by comparing their geometry with local structures.

After relocating the mainshock and early aftershocks, Wu *et al.* (2006) defined three event clusters. The first and more important cluster contains the mainshock, located under the LV and extending below the eastern border of the CER. Interestingly, its western section is extended to the south by the second cluster. Both clusters display strike-slip focal mechanisms, which are in good agreement with the main event. More precisely, Wu *et al.* (2006) defined an aftershock alignment striking N198°E and dipping steeply

Table 1
Location, Moment Magnitude, and Focal Mechanism for the Taitung Earthquake (2006)

Sources	Latitude (°N)	Longitude (°E)	Depth (km)	M_w	Focal Mechanism (Strike/Dip/Rake)
From teleseismic data					
GCMT	22.890	121.100	15.1	6.1	199/61/11 & 104/80/151
USGS	22.870	121.280	08.0	6.1	175/60/22 & 074/72/148
This study	22.892	121.078	10.8	6.1	204/80/15 & 108/78/173
From local data					
CWB	22.880	121.080	07.2		
BATS	22.880	121.080	07.2	6.1	187/76/20 & 092/71/165
Wu *et al.* (2006)	22.892	121.078	10.8	6.1	185/72/10 & 090/80/162
This study	22.892	121.078	10.8	6.1	204/50/15 & 108/78/138

Location (latitude, longitude, and depth), moment magnitude (M_w), and focal mechanisms (strike/dip/rake) are from different sources: catalogs (GCMT, USGS, CWB, and BATS, see Data and Resources), previous study (Wu *et al.*, 2006) and this paper (see text). In our study we use the location of Wu *et al.* (2006), and BATS uses the location of the CWB.

to the west (77° W) on the basis of the western section of the main cluster, which they propose as the mainshock's causative fault. However, no surface rupture confirms this association. Chen *et al.* (2009) suspected the existence of a perpendicular, secondary structure, south of the epicenter.

Linking nodal plane geometry with local structures, seismicity, and the occurrence of aftershocks is not straightforward for the Taitung earthquake. To resolve the ambiguous fault geometry, we performed a joint inversion of seismic data (from teleseismic and local strong-motion stations) and geodetic (Global Positioning Systems [GPS]) data from coseismic fault-slip distributions to test different causative fault geometries. In this study, we took advantage of seismic data that constrain fault slippage at depth to resolve the timing of rupturing, which represents a point of difference from previous studies (Wu *et al.*, 2006; Chen *et al.*, 2009), in which kinematics data alone were considered. The purpose of this study is twofold: to delineate the fault geometry and to determine the distribution of coseismic fault slip in space and time.

Datasets

For coseismic fault-slip inversion, we used two different kinds of seismic data (teleseismic and local time series) to invert jointly with geodetic data (GPS data).

For teleseismic data, we considered 29 recordings (from 22 stations; Fig. 2, left side) obtained from the IRIS data center: 19 for *P* waves and 10 for *SH* waves. All stations were located between 30° and 90° from the epicenter, selected for greatest azimuthal coverage. Each record was deconvolved from instrument response and integrated in displacement according to Nabelek's (1984) method. Separate time windows were used for *P* and *SH* waves. For *P* waves, we used a 0.01–0.80 Hz band-pass filter, a sampling time of 0.25 s, and a time window of 35 s. The same process was used for *SH* waves, except that the upper band-pass limit was reduced to 0.4 Hz. We also used a longer time sampling of 0.5 s, and a longer time window (65 s). Time windows were selected to contain direct waves (*P* and *SH*) and reflected phases (*pP* and *sP* relate to *P*; *pS* and *sS* relate to *SH*). The lengths of time windows should be long enough to include any directivity effects. A longer duration is needed to sample *S* waves, as they are characterized by longer periods. Some *P* wave records are rather noisy, making the precise determination of *P* wave arrival times difficult; consequently, those stations were given less weight in our analysis (as function of noise level). A weight of 0.5 was applied to data from the COCO and CTAO stations, and a weight of 0.25 was applied to data from the FORT and WRAB stations, permitting us to maintain station coverage to the south.

Sixteen local strong-motion stations were selected from the Central Weather Bureau (CWB, see Data and Resources) network. Coverage is asymmetrical due to the elevated and steep topography of the CER (Fig. 2, central part). East of the CER, 11 stations are located 10 km from the epicenter on average, whereas west of the CER, five stations are located about 50 km from the epicenter. As for teleseismic data, signal was integrated in displacement, and a band-pass filter of 0.05–0.50 Hz for a time sampling of 0.3 s was applied. The time window used for the inversion was adjusted depending on the station–epicenter distance, in order to contain near-field and first surface-wave arrivals (Delouis and Legrand, 1999; Delouis *et al.*, 2008).

Horizontal coseismic ground motion (from GPS data) is provided in Chen *et al.* (2009). Daily solutions from 59 stations located within 30 km of the epicenter were used in the joint inversion (Fig. 2, right side). A weight was allocated to each GPS station corresponding to its uncertainty

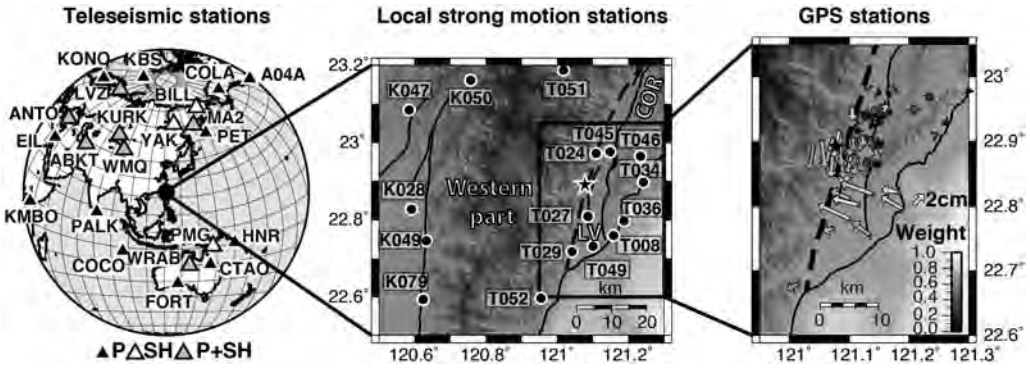

Figure 2. Locations of seismic and geodetic stations. (left) Location map of the 22 teleseismic stations (triangles). The color of triangles refers to the wave used, for which *P* is black, *SH* is white, and both *P* and *SH* are gray. The bold black circle is the epicenter of the Taitung earthquake. (center) Location of the 16 local strong-motion stations (black circles). Black lines indicate active faults. "Western part" refers to the geographic area located west of the Central Range fault (dashed black line), LV Longitudinal Valley, and COR Coastal Range. Geographic notation refers to the area separation for 1D velocity models (Fig. 3) used for modeling with local seismic data. The black rectangle corresponds to the GPS station map. (right) Horizontal coseismic ground displacement for the Taitung earthquake from Chen *et al.* (2009; arrows). The arrow color is a function of the weight applied to the data. The higher the weight, the lighter the gray-fill color. Gray circles indicate locations of the 59 GPS stations. For GPS and local strong-motion station maps, the epicenter of the earthquake is plotted as a black star.

(also provided by Chen *et al.* [2009]); the inversion favors data with the lowest uncertainties.

Search for the Focal Mechanism

As previously mentioned, the Taitung earthquake's focal mechanism is strike-slip, and no corresponding surface rupture was reported (Chen *et al.*, 2009); no robust linkage has been made between this event and any local structure. Wu *et al.* (2006) isolated the early aftershocks that define a north–south striking plane dipping steeply to the west, and associated them with the mainshock fault signature. Based on coseismic surface ground displacement (from GPS data) and on leveling data, Chen *et al.* (2009) suggested that in addition to this main structure a secondary east–west-trending fault was active during the earthquake. This second segment is located south of the epicenter, in the northern half of the Peinanshan massif.

Methods

Based on seismic data, we determined the most appropriate set of possible fault geometries to test using a joint inversion analysis. For each time series (local and teleseismic data), we performed a grid search for the defined focal mechanism parameters, using a two-step process adapted from FASTMECA (Delouis *et al.*, 2008). This method considers the source as a point source for which two parameters (strike and dip) are fixed, and the rake is inverted. Following this procedure, each category of fault geometry (i.e., each strike and dip) is associated with a best rake and waveform misfit. The misfit is quantified by the root mean square (rms) difference between observed and computed waveforms; the misfit is low for good waveform adjustments. The geometry with the lowest misfit is considered as the best solution. The grid search consists of two steps. First, strikes from 0° to 315° are tested every 45° for two different dips (45° and 90°). Second, the geometry of each previous solution is refined. In the refining process, the strike of the tested solution is varied by ±20° from the primary solution's strike. Using the best strike, dips from 15° to 75° are tested every 15° for a primary dip of 45°, or from 60° to 90° every 15° if the primary dip was 90°. If a better dip is found, the process restarts. Finally, the strike and dip of the best solution is varied every 2° by ±10° (strike) and ±10° (dip) until a geometry is obtained for which the misfit between observed and computed waveforms cannot be further improved.

Velocity Models

Synthetics were computed using Nabelek's (1984) ray theory approximation at teleseismic distance, and the discrete wave numbers method of Bouchon (1981) for local distances in a layered structure. For the teleseismic stations, we used a half-space approximation for crustal structure, with a *P*-wave velocity (V_P) of 6.0 km/s, a velocity ratio of *P* to *S* wave (V_P/V_S) of 1.73, and a density of 2.50 g/cm^3. The half-space approximation of the velocity structure cannot be used for the local dataset. Strong-motion stations are located on different types of tectonic plates: stations located to the west of the LV are on a continental plate, whereas stations east of the LV are located on an oceanic plate. As the LV is located at the boundary between two different tectonic plates, its precise structure is difficult to assess (Fig. 2, central part). Under these conditions, we expect lateral variations in V_P, V_P/V_S, and crustal thickness along the orogen; this expectation was confirmed in tomographic studies (Cheng *et al.*, 2002; Kim *et al.*, 2005, 2006; Wu *et al.*, 2007; Li *et al.*, 2009). These variations were considered in our modeling by using a specific 1D velocity model for each local strong-motion station, depending on its location within the orogen (Fig. 3). To define the models, we computed the best focal mechanism using the method described in the Methods section together with a global 1D velocity model for all of Taiwan (referred to hereafter as the global 1D model), simplified from Rau and Wu (1995). The best solution (strike/dip/rake = 205/70/40 and 93/53/155) was then fixed while processing the velocity one station at a time (the other stations being fixed by the global 1D model). Based on the processed station locations (inside the orogen), we considered several input models with increasing numbers of layers as derived from the tomographic study of Kim *et al.* (2005, 2006). For each model tested, we computed synthetic velocity models for the best focal mechanism. The misfit between observed and computed waveforms (of the processed station) is minimized by varying different parameters of the 1D velocity model. In this way, we optimized the thickness, Vp, and Vp/Vs ratio for each layer in the structure model, and retained the model that allows for the best waveform fit. The resulting 1D models are summarized in Figure 3.

Results

From the two seismic datasets (teleseismic and local were considered separately), we carried out a grid search for the focal mechanism parameters as previously explained. The results are shown in Figure 4. In addition to the best result (black triangle and beach ball), we provided solutions for waveform misfit, ranging from the best fit to those solutions with rms values of up to 2% greater than the best one. In this way, we tested the uniqueness of solutions and identified possible secondary solutions in terms of waveform misfit. We found a total of four possible solutions (strike/dip/best rake) corresponding to four nodal planes. These planes define two strike-slip focal mechanisms with a common east–west plane, but different north–south planes.

Our results (Fig. 4) are in good agreement with data from other catalogs and previous studies (U.S. Geological Survey, Global Moment Tensor Project, Broadband Array in Taiwan for Seismology, see Data and Resources, and Wu *et al.*, 2006), as shown in Figure 1 and Table 1. However, our solution from the teleseismic data suggests a more significant reverse component than does the solution from

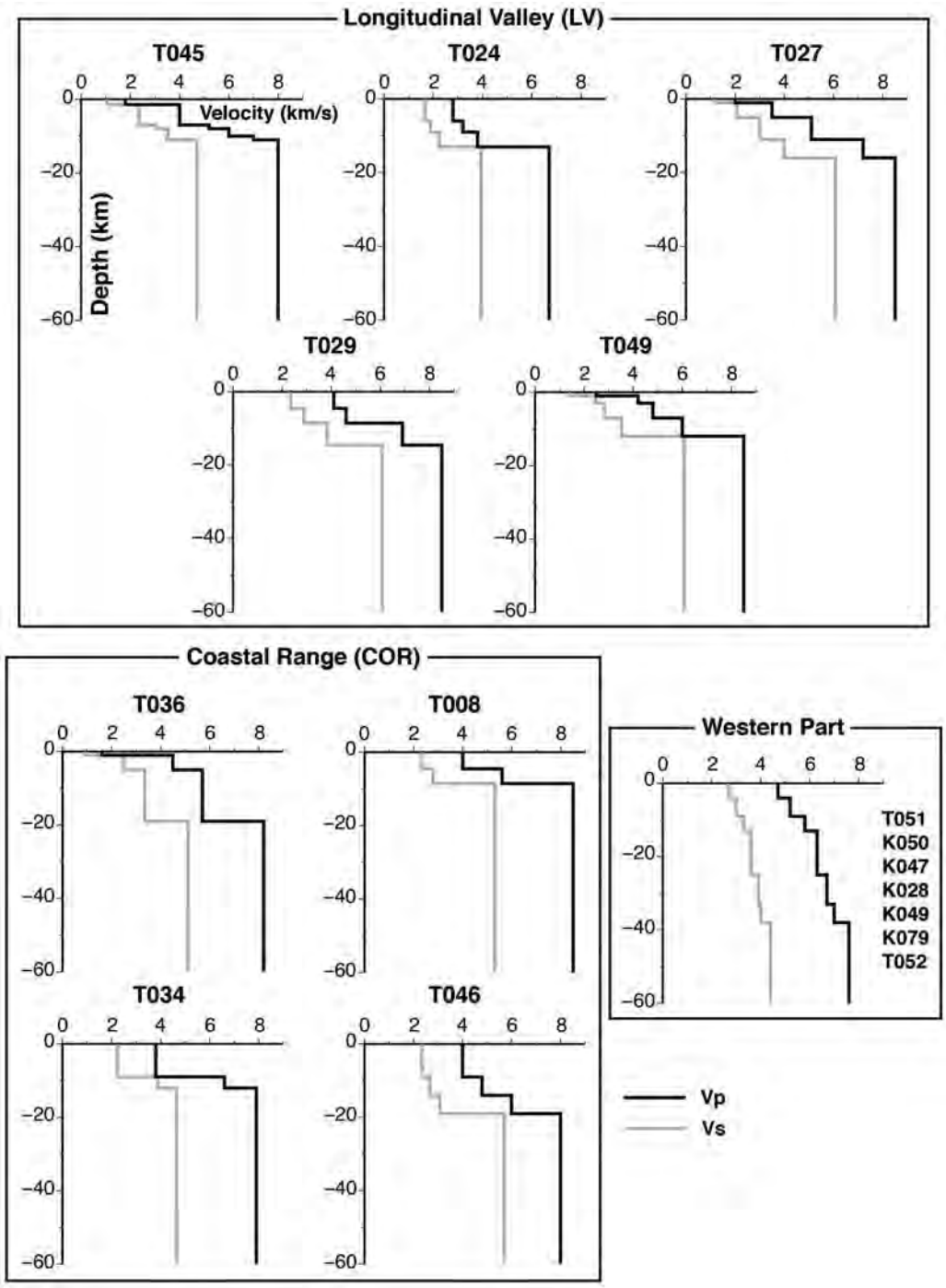

Figure 3. 1D velocity models for local strong-motion stations. A specific model is used for each station, based on the location of the station within the orogen (Fig. 2). We grouped the models into three geographic zones: west of the Central Range fault (Western Part), inside the Longitudinal Valley, and the Coastal Range. Stations in the Western Part use the global 1D model for all of Taiwan, simplified from Rau and Wu (1995). *P*-wave (V_P) and *S*-wave (V_S) velocities are plotted as black and gray lines, respectively.

the local data. This difference could indicate a variation in rake during the rupture and/or complex fault geometry. The two north–south (N204°E) planes dip to the west with a much more gentle dip (50° W) for teleseismic solutions than for local ones (80° W). Both dataset solutions have the same rake (15°), indicating left-lateral movement. Their geometry is similar to the north–south alignment described by Wu *et al.* (2006), especially for the steeply dipping planes. The east–west (N108°E) plane dips to the south (78° S) with a right-lateral rake (173°) for local data; the rake for the teleseismic data (138°) is equally reverse and right lateral. This last set of solutions can be compared with the secondary segment inferred by Chen *et al.* (2009) from geodetic data.

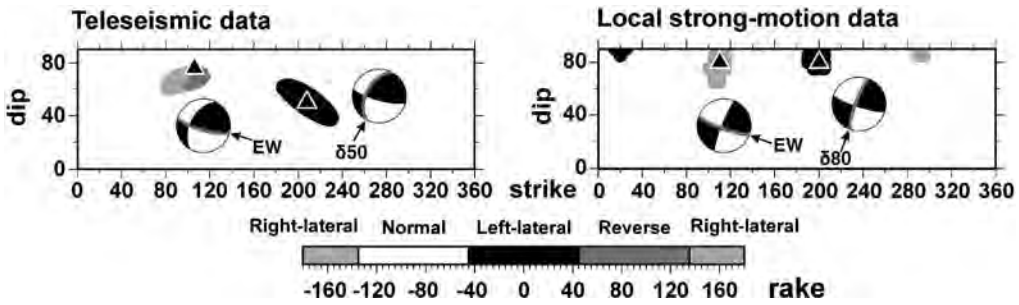

Figure 4. Results of the grid search focused on two focal mechanism parameters (strike and dip, the rake being inverted), using the two seismic datasets and shown on a strike–dip representation. Results are plotted on two separate graphs, each corresponding to one dataset. The best solutions are indicated by a black triangle. Solutions for which the waveform misfit is augmented by less than 2% with respect to the best solution are also displayed for comparison, shown with the gray shading that is a function of the rake. Teleseismic data (left side) and local data (right side) converge toward two nodal planes with the same focal mechanism. However, the two north–south planes differ in dip (steeper for the local data than for teleseismic data) whereas the two east–west planes differ in their rake (more reverse for teleseismic data).

The grid search revealed four nodal planes corresponding to three different geometries that were tested in the subsequent inversion of fault-slip distribution: one east–west striking plane dipping to the south at 78° with a variable rake; and two north–south striking planes, one dipping 50° to the west for the teleseismic data solution, and one dipping 80° to the west for the local strong-motion data solution.

Finite-Source Modeling

We separately tested the three different geometries defined to determine whether rake variation along the rupture plane could reconcile the seismic data. To improve the resolution of the fault-slip distribution, we used geodetic data of continuous GPS daily solution and campaigned GPS coseismic displacement (Chen *et al.*, 2009).

Methods

We tested three planes using the method of Delouis *et al.* (2002), for which fault displacement and rupture velocity were determined for a multisegmented fault geometry. Each segment is rectangular and subdivided into square subfaults, each 2 km in length, and for which free parameters are inverted. The location of the hypocenter is fixed and assigned to one subfault along which the rupture initiates.

The method is based on the source parameterization of time windows (Olson and Aspel, 1982) and is combined with a simulated annealing algorithm (Kirkpatrick *et al.*, 1983). The advantage of this algorithm is its ability to resolve nonlinear problems without being strongly dependent on a starting model. However, it does require *a priori* bounding values for the free parameters (Delouis *et al.*, 2002). For each subfault, three free parameters are inverted: the rake, the height of the time window (which is linked to slip on the subfault due to subfault moment release), and the rupture delay (which can vary according to two extreme rupture velocities). For the Taitung earthquake, one time window with a half-duration of 0.7 s per subfault provided the best result for modeling the time series. The convergence of the algorithm is based on the minimization of the cost function (E) that includes the rms of the misfit between observed and computed data, with additional functions concerning the total seismic moment and the smoothing of the slip distribution. The cost function also contains two kinds of weight. The first type (P_i) is attributed to the whole dataset whereas the second type (w) is assigned to each station within a dataset and is a function of the quality of the station records

$$E = \frac{\sum_1^3 P_i f}{\sum_1^3 P_i} + f_{M0} + f_s$$
$$\text{with } f = \sum_1^{\text{nstat}} w \sum_1^{\text{ntot}} \sqrt{\frac{(\text{obs} - \text{comp})^2}{\text{obs}^2}}, \qquad (1)$$

in which i refers to the data type (GPS, teleseismic, and local strong motion), f, f_{M0}, and f_s are the cost functions of data adjustment, the minimization of M_0, and the slip distribution smoothing, respectively. The two latter functions (f_{M0} and f_s) were previously described in Delouis *et al.* (2002). The data adjustment cost function (f) is computed for all station datasets (nstat) for all datapoints (ntot) recorded by each station by computing the rms difference between observed (obs) and computed (comp) data.

Another advantage of using a non-linear inversion is its ability to test a wide range of solutions before starting to converge toward the best result. We were able to determine standard deviations (σ) for the rake and the slip as in Mozziconacci *et al.* (2009). In our paper, we have extended the expression of σ to include the time delay

$$\sigma = \sqrt{\frac{\sum_{j=1}^{j=\text{nmod}} \frac{(m_{ij} - m_i)^2}{E_j}}{\sum_{j=1}^{j=\text{nmod}} \frac{1}{E_j}}}, \qquad (2)$$

in which m_i is the ith parameter of the best model, m_{ij} and E_j are the respective ith parameter and cost function of the jth model, and nmod is the number of models tested during the inversion. From the standard deviation of slip (σu), we calculated the minimum slip ($u_{\min}$) above which the slip (u) is well constrained ($\sigma u < u$). For slips larger than $u_{\min}$, the

Table 2
Geometry of the Different Models

Name	Strike	Dip	Rake	L (km)	W (km)	Number of Subfaults	Depth Range (km)
1 Segment							
EW	108	78	140 ± 50	30	18	135	2.9–19.8
δ50	204	50	40 ± 50	30	18	135	4.1–17.9
δ80	204	80	60 ± 50	30	18	135	2.1–19.9
2 Segments (2 seg)							
δ50	204	50	60 ± 50	34	12	102	8.7–17.9
δ80	204	80	70 ± 50	34	8	68	0.8–8.7
3 Segments (3 seg)							
δ50	204	50	60 ± 50	30	12	90	8.7–17.9
δ80	204	80	70 ± 50	30	8	60	0.8–8.7
EW3	110	70	130 ± 60	24	18	108	0.5–17.5

This table lists the strike, dip, rake, length (L), width (W), number of subfaults, and depth range for each model. Names are simplified as follow: EW and EW3 for the east–west segments, and δ50 and δ80 for the north–south segment that dips at 50° and 80°, respectively.

relationship between σu and u becomes linear, and the slope of the best regression line (between σu and u) gives the uncertainty in the slip (as a percentage). For subfaults with $u \geq u_{\min}$, deviations in rake and time stabilize at an average value, which we relate to uncertainties in rake ($\overline{\sigma u}$ and time ($\overline{\sigma t}$). For the time parameter, most subfaults with slips larger than $u_{\min}$ display a deviation less than $2\overline{\sigma u}$. The rupture velocity is then computed from the time delay (in s) and the distance to the hypocenter (in km) for subfaults that meet two conditions: (1) $u \geq u_{\min}$ and (2) $\sigma t \leq 2\overline{\sigma t}$. The representative rupture velocity (Vr) is the average of the subfault velocities (Vr_k) weighted by their slip (u_k). If necessary, we considered the spatial variation, Vr, by computing the average velocity for specific patches of slip on the slip map. Using the same approach, we obtain a measure of rupture velocity deviation:

$$\sigma_{Vr} = \sqrt{\frac{\sum_{k=1}^{k=n} u_k (Vr_k - Vr)^2}{\sum_{k=1}^{k=n} u_k}} \quad \text{with } Vr = \frac{\sum_{k=1}^{k=n} u_k Vr_k}{\sum_{k=1}^{k=n} u_k}. \tag{3}$$

In these expressions for σ_{Vr} and Vr, Vr_k and u_k refer to the rupture velocity and slip of the kth subfault, respectively.

Synthetic seismograms were calculated as previously described. For geodetic data, we obtained the near-field component of ground displacement using the formulation of Savage (1980), in which each subfault is considered as a dislocation surface embedded in an elastic half-space.

Fault-Slip Inversion for Three Possible Geometries

Fault model dimensions are inferred from the M_w scaling law (Wells and Coppersmith, 1994) and from previous studies (Wu *et al.*, 2006; Chen *et al.*, 2009). They are optimized in the full inversion by trial and error, and are large enough to avoid any border effect. In Table 2, we list the details for the geometries of the tested fault models; the corresponding results are given in Table 3. We simplified the plane notation by employing EW for the east–west plane, and δ50 and δ80 to distinguish the west-dipping north–south striking planes from one another.

From the inversion of EW, two main asperities were observed (Fig. 5). The deeper one is centered on the hypocenter, extends between 8 and 10 km depth and displays almost pure right-lateral movement. The shallower asperity reflects a hypocenter located in the upper 4 km of the fault model, and is purely reverse (Fig. 5). For the single δ50 plane, the

Table 3
Inversion Results for the Various Models

Name	u_{mean} (cm)	$u_{\max}$ (cm)	M_w	rms_T	rms_L	rms_G	f_{cost}
1 Segment							
EW	28	69	6.11	0.839	0.662	0.697	0.814
δ50	20	61	6.06	0.616	0.793	0.682	0.816
δ80	24	77	6.05	0.801	0.583	0.799	0.800
Combination of segments							
2 seg	31	87	6.16	0.644	0.609	0.449	0.679
3 seg	17	54	6.13	0.709	0.576	0.287	0.585

For each model, we computed the average (u_{mean}) and maximum ($u_{\max}$) slip for subfaults with slips greater than 5 cm. M_w is the moment magnitude calculated from the total moment released in the fault model. Also shown are the rms misfit for teleseismic (rms_T), local strong motion (rms_L), and GPS (rms_G) data, as well as the total cost function (f_{cost}).

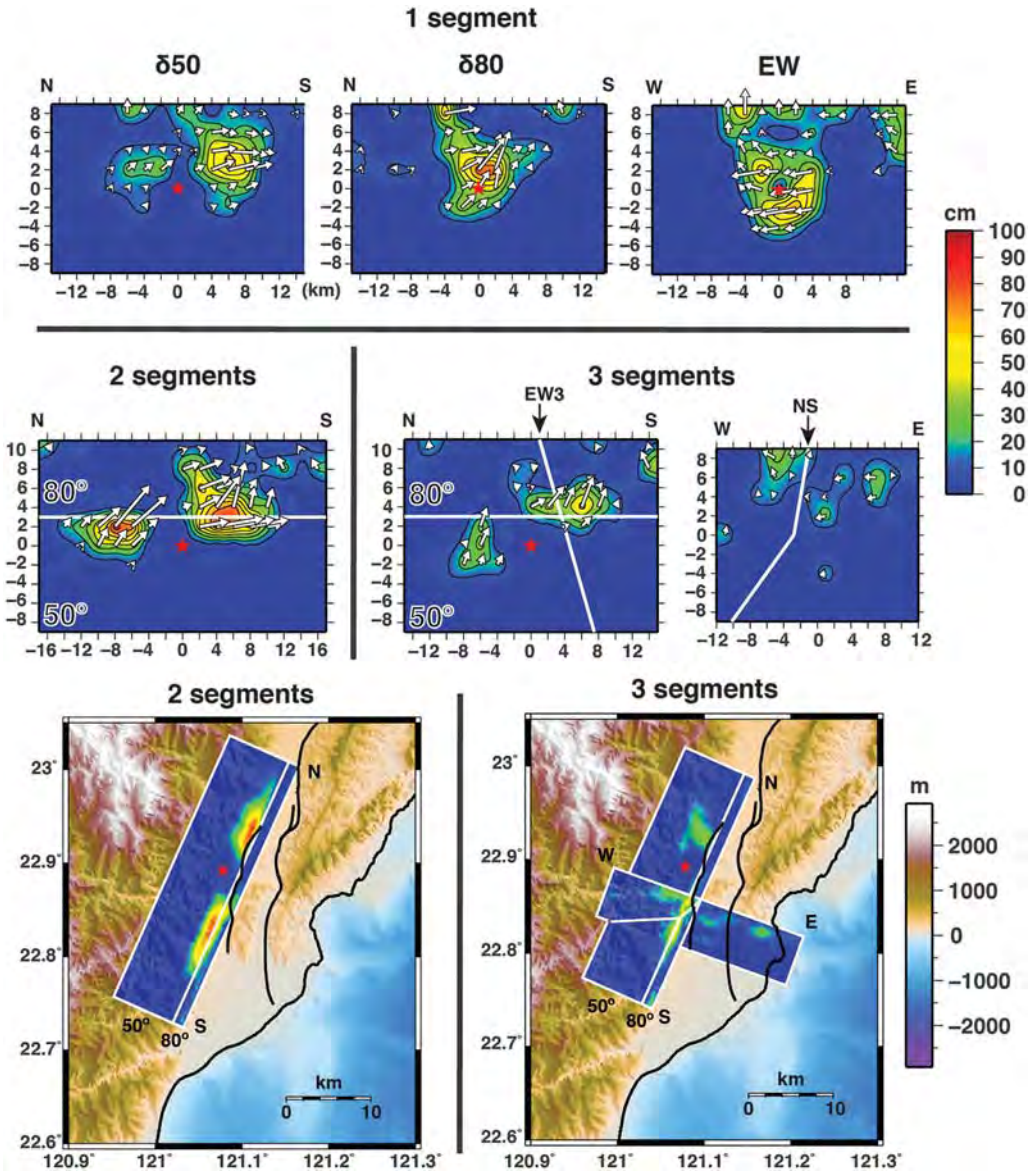

Figure 5. Slip models. (upper diagrams) Slip models for simple one-segment fault geometries: EW, east–west-trending segment; δ50 and δ80 distinguish the shallower from the steeper dipping north–south striking planes, dipping to the west at 50° and 80°, respectively. (center diagrams) Slip models for the combination of two and three fault segments (called "2 seg" and "3 seg" in the text, respectively). On the slip maps, the color scale is a function of slip and the arrows indicate the rake direction: N, north; S, south; E, east; and W, west. For the three-segment models, the intersections between the segments oriented north–south (NS) and east–west (EW3) are indicated by NS and EW3, respectively. The figures 80° and 50° refer to the dips of the north–south segments. (lower diagrams) Map view of the 2 seg and 3 seg slip maps.

rupture extends bilaterally with homogeneous left-lateral movement developing preferentially toward the south (Fig. 5). For the single δ80 plane, the rupture propagates preferentially upward. The slip direction is oblique, left lateral, with a larger reverse component than either EW or δ50 (Fig. 5). This last single-plane result is similar to the two slip maps produced by Chen *et al.* (2009; with GPS data) and to the model proposed by Wu *et al.* (2006). The same order of magnitude and average slip with a mean value of 24 cm (computed for subfaults with slips of greater than 5 cm) is observed for the three planes (Table 3). The slip maximum varies between 60 and 80 cm for a comparable moment magnitude (M_w) of 6.1. However, each model displays a non-negligible amount of near-surface slip, a finding which does not match the field observations reported by Chen *et al.* (2009).

Data adjustment of the three single planes (Table 3) shows that each plane favors one or two kinds of data among the three datasets: EW relates the local data well (GPS and local strong motion) but strongly deteriorates the teleseismic data; δ50 displays the reverse pattern, and is the only model that recovers the teleseismic data well; and δ80 displays the

best adjustment of local seismic data but fails to explain the other two datasets. None of the single-segment models is able to adequately explain all of the data. If we consider that each dataset is sensitive to different fault characteristics, then the fault geometry is more complex than a single rectangular plane. In order to determine an appropriate geometry for the causative fault, we combined the three segments. Only the best combinations, in term of data adjustment, are discussed in the following paragraphs.

Geometric Architecture from Combined Fault Segments

Two-Segment Model. For two planes, the best combination in terms of data fit is found by stacking the two north–south segments into a kinked plane (we retain the notation $\delta 50$ and $\delta 80$), with $\delta 50$ in the deeper part and $\delta 80$ in the shallower part. Thus, we obtained listric fault geometry, with decreasing dip angle with increasing depth. The best kink depth is obtained when the bend is located at a depth of 9 km (Fig. 5 and Table 2). For simplicity, we call this model 2 seg. A better result is obtained when the hypocenter is located on $\delta 50$ at a depth of 11 km, 3 km below the junction with $\delta 80$. In this configuration, the rupture initiates and propagates bilaterally on $\delta 50$ with almost purely left-lateral movement, a pattern very similar to that observed in the inversion for $\delta 50$ alone. To the south, the rupture is transmitted upward to $\delta 80$ with a simultaneously increasing thrust component, similar to that observed in the inversion for $\delta 80$ alone (Fig. 5). Consequently, 2 seg mixes the rupture characteristics of the two north–south planes with larger slip values. The mean slip is 30 cm, with a maximum of 87 cm and an equivalent M_w of 6.16 (Table 3).

Interestingly, the 2 seg model can explain equally well teleseismic and local time series data. It also greatly improves the GPS data adjustment (Table 3). In detail, local strong-motion waveforms (Fig. 6) are generally well recovered in both shape and amplitude. The same observation is found when considering the teleseismic data (Fig. 7), except that amplitudes are still underestimated. For the GPS data (Fig. 8), coseismic ground motion is well reproduced, although amplitudes are slightly lower than observed near the epicenter, and the horizontal ground movement direction deviates in a counterclockwise direction relative to the recorded one.

North–south listric geometry resolves the two seismic datasets, which is not possible using only one rectangular

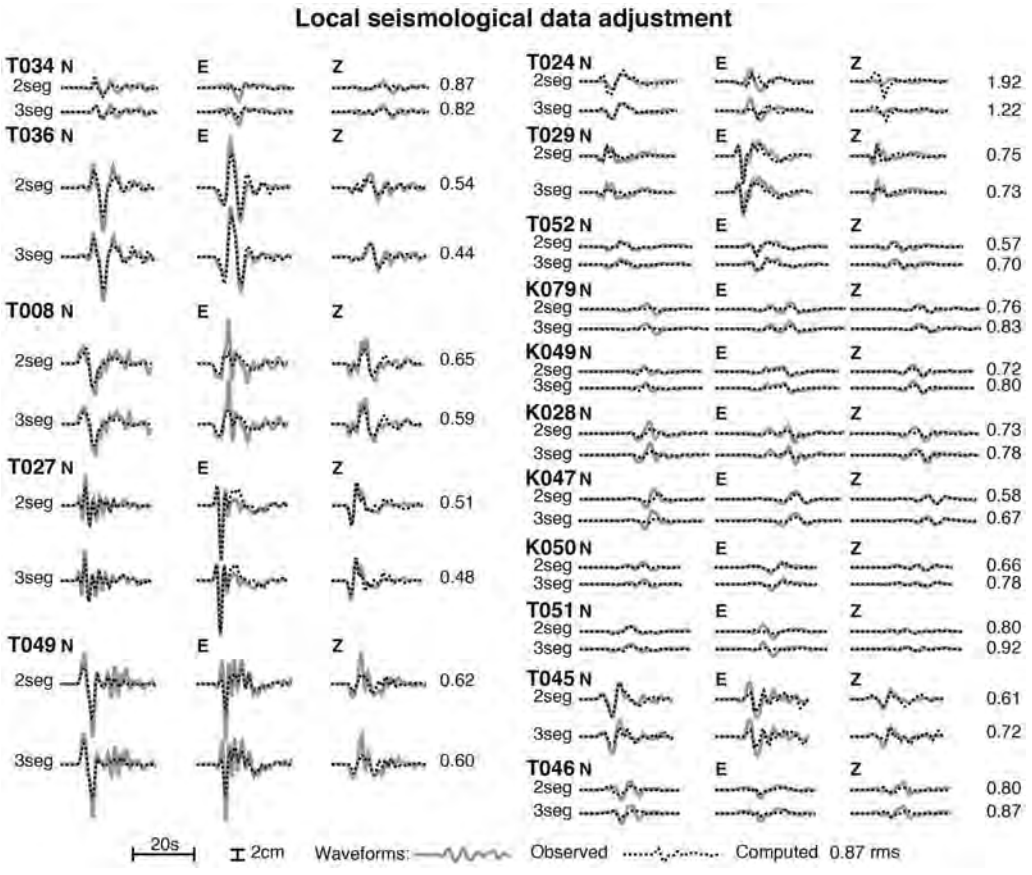

Figure 6. Local (strong motion) seismic waveform adjustment for the three components (N, north; E, east; and Z, vertical) at all stations. The observed waveform (gray) is compared with the calculated one (black and dotted line) for 2 seg and 3 seg. The horizontal scale is always 20 s and the vertical scale is 2 cm. The number next to the Z component of each station specifies the misfit between the observed and computed waveform (normalized rms).

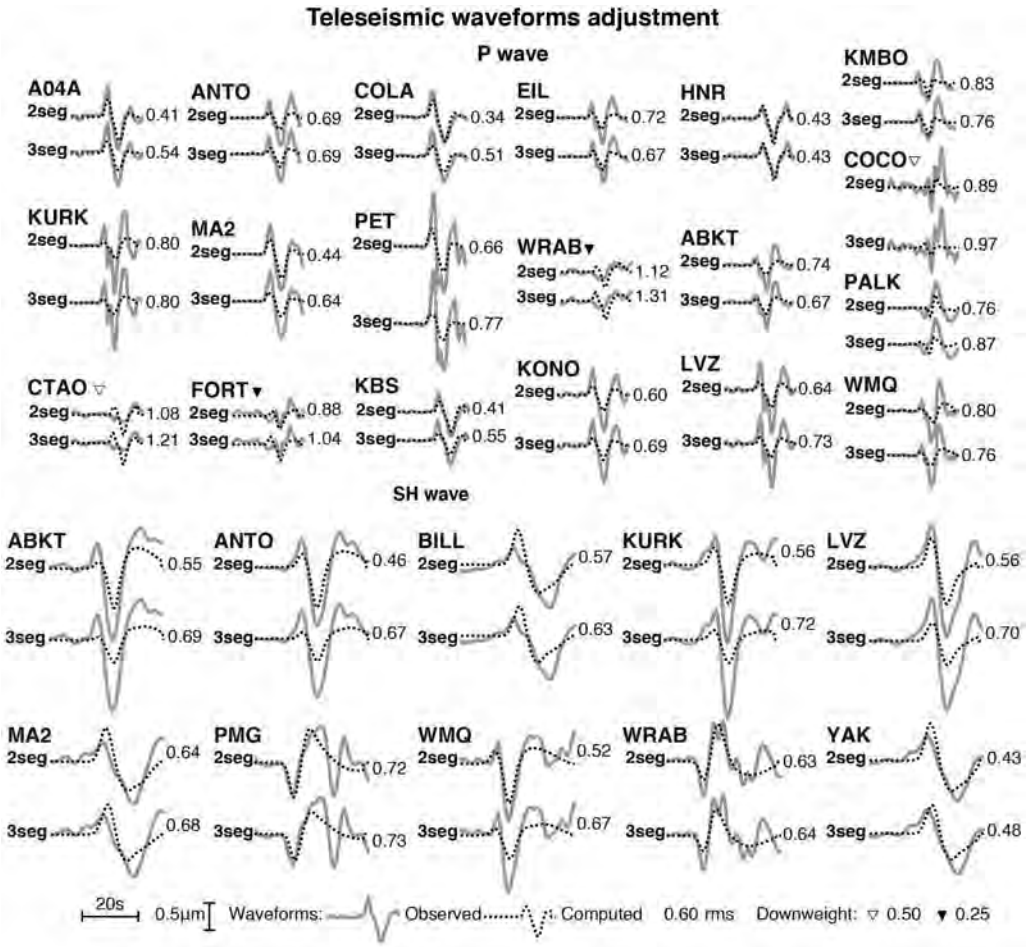

Figure 7. Teleseismic waveform adjustment for *P* and *SH* waves. See Figure 6 for the legend, although the vertical scale is 0.5 μm.

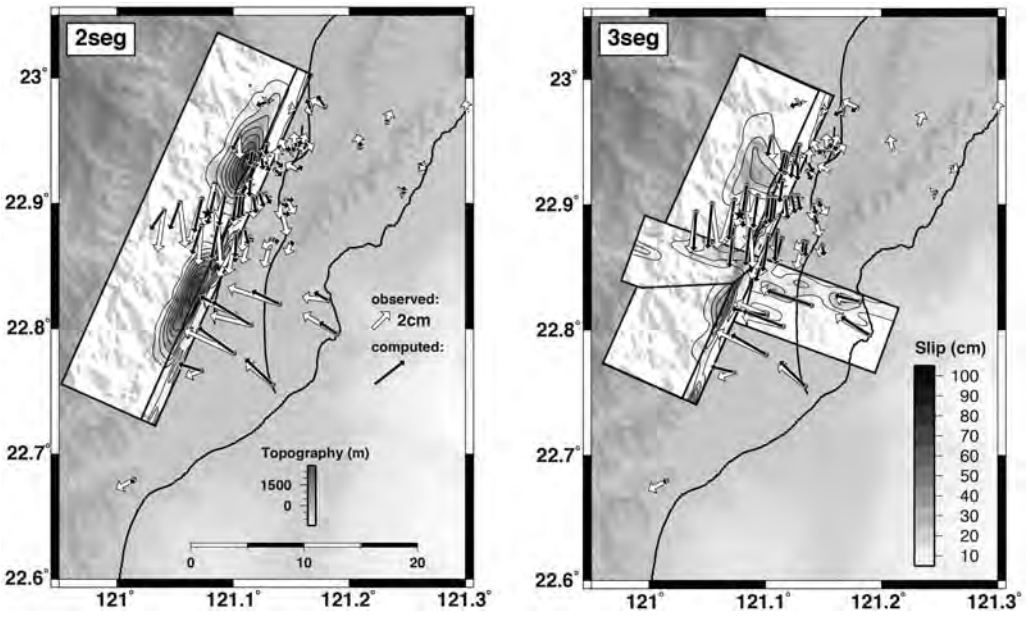

Figure 8. GPS data adjustment. White arrows indicate the observed coseismic horizontal displacement to be compared with the displacement calculated (black arrow) from models 2 seg (left) and 3 seg (right). The surface projection of the modeled fault-slip distributions is plotted in gray scale, above a shaded topography. The epicenter of the Taitung earthquake is marked as a black star.

fault segment. Model 2 seg provides a global data adjustment that is good enough to suggest that this listric geometry is the effective one. However, we also test the proposal of Chen *et al.* (2009), with coexisting east–west and north–south structures.

Three-Segment Model. The last fault geometry tested combines all three planes (model 3 seg). The three-segment geometry that best explains all of the data is obtained by combining the previous 2 seg model with a cross-cutting east–west segment, similar to EW (and named "EW3" hereafter), south of the hypocenter. In this configuration, the geometry and location of EW3 was slightly modified in order to optimize the fit of the GPS data (Table 2). The resulting rupture reproduces the main characteristics of the 2 seg model, but with lower slip amplitude. Along the EW3, the principal sense of displacement is right lateral and is concentrated in the shallower portion of the segment, near the intersection with $\delta 80$ (Fig. 5). The average slip (17 cm) for the overall model is smaller than for other configurations, with a maximum slip of 54 cm for a corresponding M_w of 6.13 (Table 3).

The only geometrical difference between 2 seg and 3 seg is the addition, in 3 seg, of the EW3 segment. The north–south listric structure is identical in both models. To determine whether EW3 is one of the structures activated during the earthquake, we compared the data adjustments obtained using the 2 seg and 3 seg models.

The overall misfit of each dataset (Table 3) indicates that 3 seg improves local data, especially GPS data, but deteriorates teleseismic data, reproducing the inconsistencies observed in seismic data for the one-segment models, though at a lower level.

In detail, the shapes and amplitudes of local strong-motion waveforms (Fig. 6) are well recovered in both models. However, 2 seg is the only model to allow for the correct reproduction of all near-station polarities. Polarity deterioration of first arrival in the 3 seg model (the *Z* component of stations T034, T029, and T052, and the *E* component of station T024) is due to the modification of the slip distribution on north–south (NS) close to the hypocenter (Fig. 5). The two asperities display a variation in shape, with lower amplitudes, and are also located slightly farther from the hypocenter when compared with the 2 seg model. These observations reinforce our statement that the 2 seg model (a west-dipping, north–south-trending listric plane) represents the optimum geometry for coseismic rupturing associated with the Taitung earthquake. For teleseismic data (Fig. 7), the differences between the two models lie predominantly in the waveform amplitude, which is almost always underestimated in 3 seg. Because the two models display the same slip patterns along their common north–south segment, with less slip for 3 seg than for 2 seg, we propose that the greater slip range in 2 seg offers a better explanation of the earthquake.

Seismic data (local and teleseismic) seem to favor the north–south listric plane alone (2 seg), rather than in combination with a secondary east–west plane (3 seg). However, GPS data support the opposite conclusion (Fig. 8), for which the 3 seg model better explains the coseismic ground-displacement features. Concerning GPS ground displacement, the difference between the two models appears mostly for stations that are located near the epicenter (Fig. 8). In this area, 3 seg is able to recover both the amplitudes and direction of GPS data by the addition of faulting along EW3.

Selection of the Optimal Geometry

In contrast with the one-segment models, 2 seg and 3 seg do not produce significant slip at the surface, which is in agreement with field observations (Chen *et al.*, 2009). Comparing the data adjustments of the two latter models, we conclude that the GPS data need EW3 only to explain the large amplitudes from the southeastern stations, and the displacement orientations of the western ones. However, to account for teleseismic waveforms and some records from local stations near the epicenter, larger slips along the listric north–south segment are needed. This slight discrepancy between seismic and geodetic data may be due to the recording time. Seismic time series record the first minutes of the event, whereas GPS data were obtained by processing daily records for a few continuous GPS stations and determining the coseismic displacements for the remaining campaigned GPS stations (Chen *et al.*, 2009), which can therefore be contaminated by very early after-slip events. Before making assumptions about co- and/or post-seismic activation along EW3, we evaluated whether simultaneous slip along the listric north–south fault and EW3 could be effectively detected using our datasets.

Resolution Tests

Synthetic Model

Using a synthetic model, we aimed to test the ability of our data to retrieve a reliable slip distribution for a complex geometry, as in 3 seg. More precisely, we tested whether the station coverage was sufficient to recover the characteristics of the observed rupture process obtained from the real data, given the fault geometry. Each type of fault geometry was tested, but only the most complicated test (3 seg geometry) is presented here, as it resolves the question of whether simultaneous slip can be detected on cross-cutting planes.

The test geometry and the slip pattern (Fig. 9, upper part) used are based on the results of 3 seg (Fig. 5). We imposed three slip patches with uniform displacements (50 cm) and varied the rake and rupture velocity. The northern slip patch (N in Figs. 9 and 10) has a rake of 50° for a rupture velocity of 1.4 km/s, whereas the southern (S) and the western (W) patches both propagate at a faster rate of 2.4 km/s with different rakes (90° and 130°, respectively). From this model we calculated corresponding seismic and geodetic data, which were input into the following inversions.

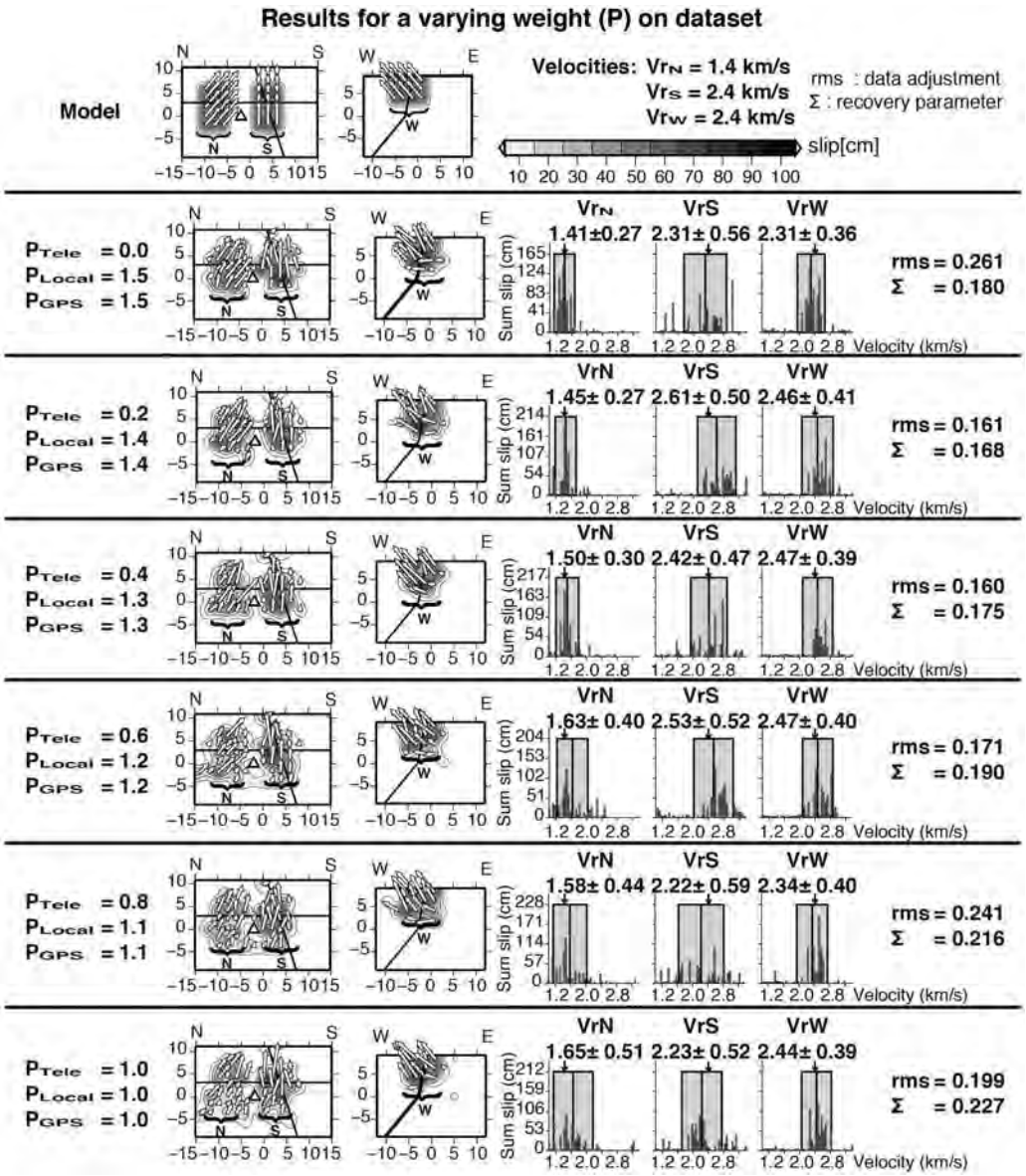

Figure 9. Test of weighted datasets using a synthetic model and data. For each test on the weighted dataset, we provide from left to right: the global dataset weight used (P_{TELE}, teleseismic data; P_{LOCAL}, local strong motion; P_{GPS}, GPS data), the slip pattern along the north–south listric structure (NS) and on EW3 (WE; the intensity of gray depends on the slip), and rupture velocities in the three slip patches (Vr_N, Vr_S, and Vr_W). For each velocity, the dispersion of Vr is shown within the corresponding slip patch (see the text for more information). To the right of each test is shown the data misfit (rms) and the recovery parameter (Σ; each to be minimized).

Weighted Data

One of the subtleties of joint inversions involving differing kinds of datasets is their global weight (P_i). This weight differs from the internal weight (w) attributed to the stations. The internal weights (w) quantify the quality of a record whereas the global weight (P_i) balances the importance of a dataset relative to the two other datasets. We performed several tests in order to retrieve the best weight combination that accurately provides both the slip pattern and the rupture timing, knowing that the finite-slip distribution is mainly constrained by local data (local strong-motion and GPS data) whereas its temporal evolution is assessed from seismic data. In our test, we kept a constant sum of three for the total weight of the three datasets and investigated more specifically the weight of the teleseismic data (for which the resolution power is the lowest, as discussed in the following paragraph) from 0.0 to 1.0 at steps of 0.2 (Fig. 10). The best configuration provides a good data fit and recovery of both the slip pattern and the rupture timing. Consequently, in addition to the data fit, previously expressed by the rms on data misfit, we considered recovery of both the slip pattern and the rupture timing as follows:

$$\Delta X = \frac{\sum_1^n (X_{\mathrm{synthetic}} - X_{\mathrm{computed}})^2}{\sum_1^n X_{\mathrm{synthetic}}^2}, \qquad (4)$$

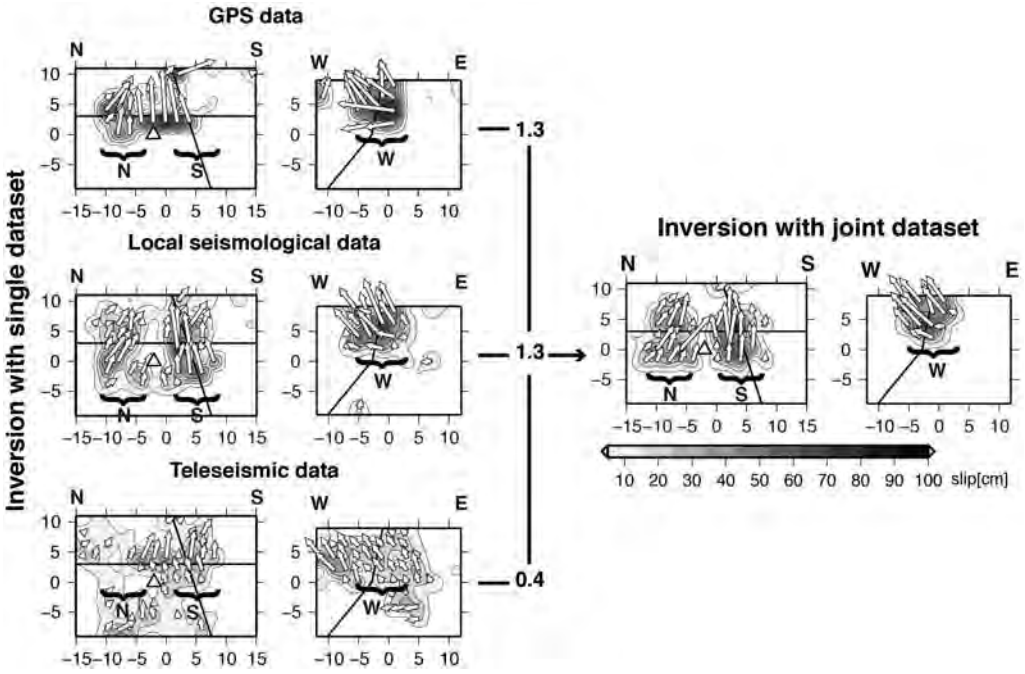

Figure 10. Synthetic tests carried out with a single dataset and by a joint inversion. We performed inversions using individual datasets (left) and the joint inversion of the three datasets (right). The slip pattern of the synthetic model is the same as in Figure 9 (top). The gray scale is a function of slip (cm). Between single dataset inversions the right part of the figure, the general weight (P_i) of datasets is indicated (see Fig. 9 and the text).

in which X is either the slip (ΔX_{slip}), the rake (ΔX_{rake}), or the time delay (ΔX_{time}), and n is the number of subfaults. For the rupture timing, we determined the rupture velocity (Vr) and its corresponding deviation (σ_{Vr}) for the three slip patches, as previously defined. Then, we considered the difference between calculated and synthetic rupture velocities (Δv):

$$\Delta v = \frac{\sum_1^3 \sigma_{Vr}(Vr_{\text{synthetic}} - Vr_{\text{computed}})^2}{\sum_1^3 \sigma_{Vr} V_r^2}. \qquad (5)$$

The recovery parameter (Σ) is simply the sum of ΔX and Δv: $\sum = \frac{\Delta X_{\text{slip}} + \Delta X_{\text{rake}} + \Delta X_{\text{time}}}{3} + \Delta v$.

Figure 9 displays the results of the joint inversions for varying weights on datasets. A good correlation was found between improvement in the data fit (low rms) and acceptable model recovery (low Σ). The best weight combination was obtained by downweighting the teleseismic data by 0.2 and 0.4. Both configurations give similar results. However, although weighting the teleseismic data by 0.4 results in a slight deterioration in the resolution of the slip pattern (when compared with 0.2), it significantly improves the resolution of the rupture timing and is taken as the best compromise. Thus, for all inversions presented in the paper, we adopted this weighting combination, with a weight of 0.4 for the teleseismic dataset.

Final Results

The results of slip distribution obtained from inversions using the best weight combinations are illustrated in Figure 10. We also provided the results of the single dataset inversions for comparison, which support the advantages of the joint-inversion method.

With GPS data, the two slip patches along the north–south segment were amalgamated and flattened just beneath the junction of $\delta 80$ with $\delta 50$. This recovery problem is due to the lack of stations in the southwestern portion of our study area. However, the slip pattern along EW3 is well reconstructed, although its amplitude is overestimated. Local strong-motion data give the best result among the single dataset inversions. The slip pattern is well retrieved along all segments, with a notable distinction between the northern and southern slip patches on the north–south segment. Conversely, the teleseismic data poorly constrained the slip pattern, but were remarkably sensitive in respect of rupture timing. When datasets are considered together in the inversion, the slip pattern and the rupture timing are both recovered properly. The joint inversion of seismic and geodetic data not only provided a noticeable improvement in the recovery of the slip pattern, but was also able to detect variation in rupture velocity (Figs. 9 and 10).

This test demonstrates that our data configuration can discern two simultaneous ruptures along cross-cutting planes (EW3 and north–south segments) even if the rupture is complicated by a variation in its propagation velocity. In addition, the signal emitted by EW3 occurred during the first 15 s of local strong-motion recording, lasting at least 10 s. This period corresponds to the largest amplitude. Because the criterion to model waveforms is to minimize the difference between observed and computed waveforms, the inversion

tends to better adjust large amplitudes. In other words, if a non-negligible slip occurred along the EW3 while seismic data were being recorded, those data would be significantly improved by incorporating EW3 in the fault model. Because this was not observed, we infer that no substantial slip occurred along this segment during the earthquake. It is possible that late activation occurred along EW3, after seismic data were recorded. This late faulting probably did occur, as indicated by the substantial improvement in the GPS data when EW3 is included in the modeling.

Details of the Main Fault Rupture

Standard Deviation

As mentioned in the Methods section, we calculated the standard deviation for the free parameters of the inversion and the rupture velocity (Fig. 11). The uncertainty in slip was obtained from the relationship between slip (u) and slip deviation (σu) (Fig. 11a). Slips with displacements of greater than 5 cm ($u_{\min}$) are constrained ($\sigma u < u$), and a linear relationship exists between σu and u. The slope of the regression line gives the uncertainty on u, which is 32% for this model. The σu on the map (Fig. 11a) confirms that the greatest deviations are obtained for the largest slips. As previously mentioned, we calculated average standard deviations for the two remaining free parameters of the inversion (rake $\overline{\sigma r}$ and time delay $\overline{\sigma t}$) for subfaults with slips greater than $u_{\min}$. The data in Figure 11b,c justify the use of an average, because σr and σt stabilize at constant values of 10.9° and 0.54 s for the rake and time delay, respectively. We provided a map of σr and σt (Fig. 11b,c) Both maps show the greatest deviations for subfaults with slips of less than 10 cm, supporting the use of $u_{\min}$ as the lower limit for subfault to be constrained. In other words, all three of the free parameters are resolved when $u \geq u_{\min}$, with $u_{\min}$ being the minimum slip that our data can resolve.

In the case of rupture velocity Vr (Fig. 11c,d), we restricted our computation to subfaults with $u \geq 5$ cm and $\sigma t \leq 2\overline{\sigma t}$. Because two slip patches are shown on the slip map (N and S in Fig. 11), we determined their specific rupture velocities separately in order to detect any spatial variation related to Vr. For each subfault, we calculated corresponding values for Vr using the distance from the

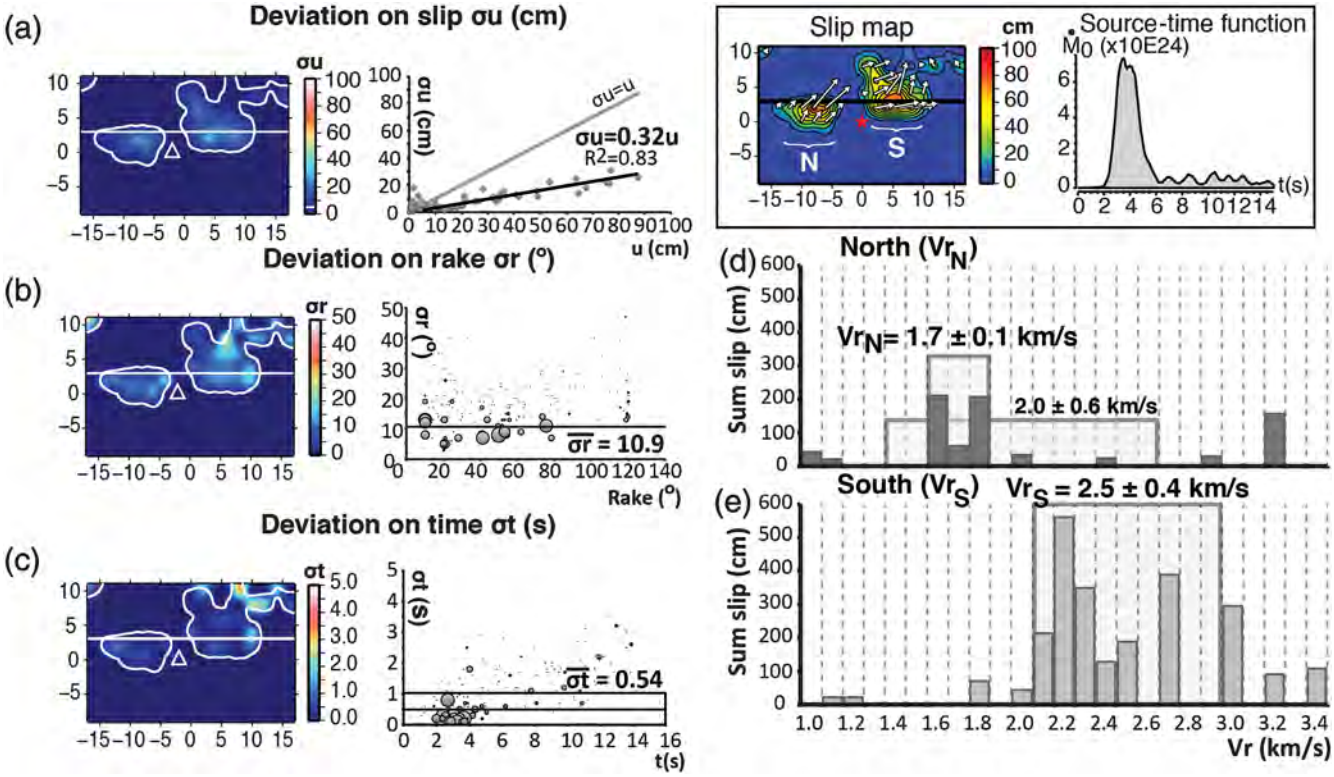

Figure 11. Deviation of free parameters and Vr. (left) (a) Deviation on slip, (b) rake, and (c) time delay. Deviation maps are restricted to subfaults with slips of greater than 5 cm (see text). The color scale is a function of the deviation intensity. White curve: 5 cm slip contours. White triangle: hypocenter. Next to each map, a graph of the deviation is plotted as a function of its corresponding parameter. For slip, a linear relationship between σu and u is obtained for values of $u \geq 5$ cm, with a slope of 32%, and a regression coefficient R^2 of 0.83. Gray line: $\sigma u = u$. For rake and time, the diameter of gray circles is a function of slip. Black line: average deviation of the rake ($\overline{\sigma r}$) and the time delay ($\overline{\sigma t}$). For the time only, the domain for which $\sigma t \leq 2\overline{\sigma t}$ is plotted as a black rectangle. Frame: slip map with slip patches where N is the northern asperity and S the southern asperity (model 2 seg). The source-time function (STF), which is the moment-rate ($\dot{M}_0$, in dyne-cm/s) release as a function of time (s), is also plotted. The STF displays one main release between 2 and 6 s. (right) Rupture velocity dispersion as a function of the slip for each slip patch: (d) Vr_N for N and (e) Vr_S for S. The uncertainty for each Vr is indicated by a gray rectangle.

hypocenter and time-delay information, plotting the results on a histogram of Vr intervals. For each interval, we summed the slips for each subfault with the corresponding rupture velocity. Vr was found to vary from 1.0 to 3.4 km/s (every 0.1 km/s), which are the bounding values of the rupture velocity set *a priori* in the inversion. To the north (Fig. 11c), the rupture velocity (Vr_N) yielded an average value of 2.0 ± 0.6 km/s. However, this value is strongly influenced by the existence of a small group of subfaults with extreme velocities. When these extreme values were removed from the computation, Vr_N is restricted to 1.7 ± 0.1 km/s, which is in agreement with the northward rupture propagation shown in Figure 12. Finally, to the south, the rupture velocity (Vr_S in Fig. 11d) is straightforward to determine, because there are no extreme values to compromise the average; the result is a Vr_S of 2.5 ± 0.4 km/s.

In the Rupture Propagation section, we describe the propagation of the rupture in detail, in terms of its spatial and temporal variation (Fig. 12).

Rupture Propagation

The source-time function (Fig. 11) indicates a single episode of moment release between 2.0 and 6.0 s. In this time interval, we determined that a bilateral rupture was initiated, with a greater southward velocity (2.5 ± 0.4 km/s) than northward (1.7 ± 0.1 km/s). Snapshots of the rupture (Fig. 12) illustrate the propagation of the rupture from the hypocenter (on $\delta 50$), developing significant slip after $T = 2.0$ s for subfaults located near the junction between $\delta 50$ and $\delta 80$. The rupture was then quickly transmitted upward to $\delta 80$ in the south (at $T = 2.5$ s), while remaining confined to $\delta 50$ in the north. Interestingly, the southward rupture displays the greatest amount of slip along both sides of the limit between $\delta 50$ and $\delta 80$, and at the intersection with EW3 (dashed white line in Fig. 12).

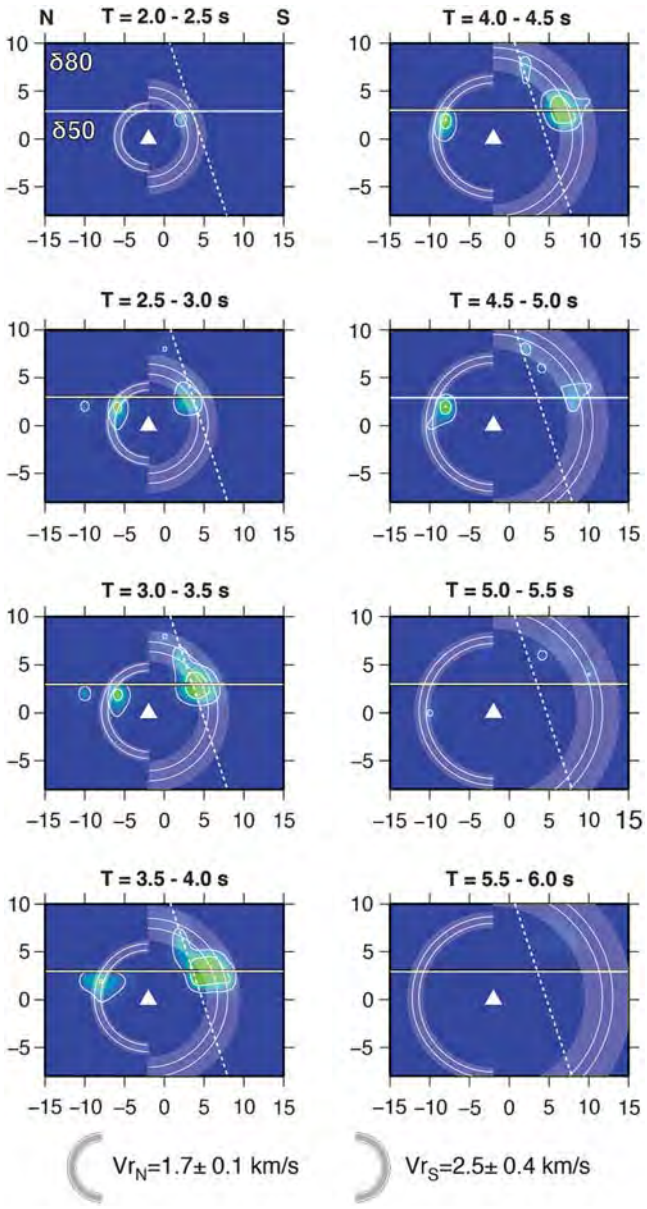

Figure 12. Snapshots of rupture propagation for 2 seg. Snapshots sample the main moment rate release (see Figure 11) that occurred between 2 and 6 s after the rupture was initiated. In the first slip map ($T = 2.0$ s), we show the orientation of the fault plane (N, north; S, south). White horizontal line: segment boundary between $\delta 50$ and $\delta 80$. White dashed line: intersection of $\delta 50$ and $\delta 80$ with EW3 in 3 seg, for comparison. White triangle: hypocenter. Each snapshot shows slip contour lines (every 5 cm). We mapped the asymmetrical rupture front for the northward rupture that develops at $Vr_N = 1.7 \pm 0.1$ km/s and the southern one at $Vr_S = 2.5 \pm 0.4$ km/s by white shaded half-donuts. The donut width corresponds to the location domain of the rupture according to the time period of the snapshot (0.5 s length) and the corresponding rupture velocity and associated uncertainty. To simplify the figure, the total length of the triangular time window (2×0.7 s) is not shown.

Discussion and Conclusion

From the grid search for focal mechanism parameters using teleseismic and local strong-motion data, we found two similar strike-slip focal mechanisms with variation in the reverse component, implying a change of rake during the rupture and/or complex fault geometry. The two north–south nodal planes have the same strike but different dips, whereas the two east–west plane alternatives differ only in their rakes. As a result, only three different fault geometries exist that could explain the Taitung earthquake.

The effective fault geometry was further constrained by testing the three fault models by jointly inverting seismic and geodetic data. However, we found that these simple models could not explain all three datasets; we propose a more complex structure, in which the initial planes are combined. Finally, only two models remain to explain the earthquake. Both models consider a west-dipping north–south-striking listric fault. This main structure was considered alone (2 seg) and in association with a cross-cutting east–west segment (3 seg). The resolution power of 3 seg was tested, and

the results indicate that simultaneous slip along these cross-cutting structures can be discriminated. Because the additional east–west segment does not improve waveform modeling, we infer that the main fault (2 seg) was likely active alone during the mainshock; movement along an east–west segment is supported solely by GPS data. However, the large improvement to the fit with the geodetic data suggests that the east–west segment was possibly active shortly after the main event, contaminating the GPS data.

A 6-s long rupture event was derived from the seismic data. In detail, the rupture was initiated along the lower segment of the fault (dip 50°) before propagating bilaterally with an average slip of 30 cm and a maximum slip of 87 cm (with an uncertainty of 32%). In either direction, the greatest amount of slip occurs near the slope break of the kinked north–south fault. Interestingly, the rupture remains confined to the lower segment in the north, while being rapidly transmitted to the upper segment (dip 80°) in the south, where it also propagates at a slightly faster velocity (2.5 ± 0.4 km/s compared with 1.7 ± 0.1 km/s for the northward propagation).

Another aspect of the rupture is its pattern in the southern portion of the fault model, where the slip is transmitted to the upper segment. There, it is collocated with the proposed junction with the east–west plane of the 3 seg model (EW3; Fig. 12). Because EW3 mainly improves only GPS data, we infer that during the mainshock this segment did not rupture significantly but helped the rupture propagate upward along the main north–south structure. Then, shortly after the mainshock, additional slip took place along EW3. This difference in activation time could explain why this late movement only affected the GPS data. Comparing our findings with early aftershock data, the two main aftershock event clusters isolated by Wu *et al.* (2006) are located on either side of EW3, with the southern cluster being much less active than the northern one. This abrupt difference in seismic activity while the rupture continued to propagate farther south provides additional evidence to support the existence of EW3. Moreover, its existence is also proposed in Yu and Hung (2012) to explain temporal changes in crustal velocity at shallow depths, resulting from the same earthquake. In their study, only stations located near the junction between EW3 and NS display a significant velocity drop.

Finally, we point out the link that exists between our fault model and local geological structures. The main listric fault dips to the west, a geometry that is in agreement with the geometry inferred for the CRF (Shyu *et al.*, 2006, 2008). It follows that the Taitung earthquake can be attributed to movement along this structure. Our study identifies listric geometry for this fault, which was previously modeled as a simple north–south-trending, west-dipping, rectangular plane. The CRF was previously described not only as a backthrust (Biq, 1965; Shyu *et al.*, 2006), but also as a probable major strike-slip fault because left-lateral shear deformation was observed to dominate the eastern flank of the Central Range (Yeh *et al.*, 2001; Fisher *et al.*, 2002). Thus, it is not surprising to discover that complex coseismic slip is responsible for the Taitung earthquake, for which the mechanism was mainly from strike-slip motion, except in the southern part of the rupture where the movement was predominantly reverse. As noticed previously, the CRF remained dormant (or locked) prior to the Taitung earthquake, with no record of any large earthquake prior to this event. Thus, its potential behavior during a large event is still unknown, assuming that the Taitung earthquake was a relatively moderate event. Short-term earthquake-related faulting and long-term geological faulting can differ because the type of faulting depends on whether a large or a small event activates a fault segment. Such variation was observed along, for example, the Karadere fault, a segment of the North Anatolian fault. Movement along this fault was purely right lateral during the 1999 Izmit earthquake (M_w 7.4) in Turkey, although previously it had exhibited purely reverse movement during an earthquake (M_w 4.9) experienced one month before (Seeber *et al.*, 2000). Correspondingly, the faulting observed for the Taitung earthquake is not incompatible with geological records on the CRF, making this event the first large earthquake ever recorded for this structure. The Taitung earthquake was followed by another event, 15 days later, an earthquake with the same order of magnitude and for which the epicenter was located offshore, 15 km east of the first event. This latter event will be the topic of further study.

In conclusion, although this earthquake was of moderate magnitude (M_w 6.1), it involved complex fault geometry, with cross-cutting segments and differing time periods of activation. This fault behavior has complicated our view of moderate earthquakes, revealing a complexity that should be more widely studied.

Data and Resources

Seismic data from teleseismic stations are from the Incorporated Research Institution for Seismology (IRIS) consortium Data Management Center (DMC) (http://www.iris.edu, last accessed November 2010). Data from the local region are from the Central Weather Bureau (CWB; http://www.cwb.gov.tw/eng/, last accessed June 2012). GPS data were those of Chen *et al.* (2009). Earthquake focal mechanisms are from the Global Moment Tensor Project (GCMT) and from the U.S. Geological Survey (USGS) teleseismic networks, and can be obtained from http://earthquake.usgs.gov/earthquakes/eqarchives/sopar/ (last accessed November 2010). Mechanisms for local data are from Broadband Array in Taiwan for Seismology (BATS; http://tecws.earth.sinica.edu.tw/BATS/cmtbyform.php, last accessed June 2012) and from Wu *et al.* (2006).

Acknowledgments

We would like to dedicate this paper to J. Angelier, who initiated this study. We also thank S. J. Lee, Y. J. Hsu, and W. C. Yu for invaluable discussions. This research was supported by the Institute of Earth Sciences, Academia Sinica, and the ORCHID (Minitère des affaires étrangères) and LIA (INSU-CNRS-NSC) projects. This work was also supported by the

Taiwan Earthquake Research Center (TEC) funded through National Science Council (NSC) with Grant Number NSC 99-2116-M-001-022. The TEC contribution number for this article is 00088.

References

Angelier, J., H.-T. Chu, J.-C. Lee, and J.-C. Hu (2000). Active faulting and earthquake hazard: The case study of the Chihshang fault, Taiwan, *J. Geodyn.* **29,** 151–185.

Barrier, E., and J. Angelier (1986). Active collision in Eastern Taiwan: the coastal range, *Tectonophysics* **125,** 39–72.

Barrier, E., J. Angelier, H.-T. Chu, and L.-S. Teng (1982). Tectonic analysis of compressional structure in an active collision zone: The deformation of the Pinanshan Conglomerates, eastern Taiwan, *Proc. Geol. Soc. China* **25,** 123–138.

Biq, C. (1965). The east Taiwan rift, *Petrol. Geol. Taiwan* **4,** 93–106.

Biq, C. (1972). Dual trench structure in Taiwan-Ryukyu region, *Proc. Geol. Soc. China* **15,** 65–75.

Bouchon, M. (1981). A simple method to calculate Green's functions for elastic layered media, *Bull. Seismol. Soc. Am.* **71,** 959–971.

Chai, B. H. T. (1972). Structure and tectonic evolution of Taiwan, *Am. J. Sci.* **272,** 389–422.

Chen, H.-Y., Y.-J. Hsu, J.-C. Lee, S.-B. Yu, L.-C. Kuo, Y.-L. Jiang, C.-C. Liu, and C.-S. Tsai (2009). Coseismic displacements and slip distribution from GPS and leveling observations for the 2006 Peinan earthquake (M_w 6.1), *Earth Planets Space* **61,** 299–318.

Cheng, W.-B., C. Wang, C.-T. Shyu, and T.-C. Shin (2002). Crustal structure of the convergent plate-boundary zone, eastern Taiwan, assessed by seismic tomography, in *Geology and Geophysics of an Arc-Continent Collision, Taiwan, Republic of China*, T. B. Byrne and C.-S. Liu (Editors), Vol. **358**, Spec. Pap. Geol. Soc. Am., Boulder, Colorado, 163–178.

Delouis, B., and D. Legrand (1999). Focal mechanism determination and identification of the fault plane of earthquakes using only one or two near-source seismic recordings, *Bull. Seismol. Soc. Am.* **89,** 1558–1574.

Delouis, B., C. Charlety, and M. Vallée (2008). Fast determination of earthquake source parameters from strong motion records: M_w, focal mechanism, and slip distribution, Presented at *EGU General Assembly*, Geophys. Res. Abstr. 10, Abstract 04939, Vienna.

Delouis, B., D. Giardini, P. Lundgren, and J. Salichon (2002). Joint inversion of InSAR, GPS, teleseismic, and strong-motion data for the spatial and temporal distribution of earthquake slip: Application to the 1999 Izmit mainshock, *Bull. Seismol. Soc. Am.* **92,** 278–299.

Fisher, D. M., C.-Y. Lu, and H.-T. Chu (2002). Taiwan slate belt: Insights into the ductile interior of an arc-continent collision, in *Geology and Geophysics of an Arc-Continent Collision, Taiwan*, T. Byrne and C.-S. Liu (Editors), Vol. **358**, Spec. Pap. Geol. Soc. Am., 93–106.

Ho, C.-S. (1986). A synthesis of the geologic evolution of Taiwan, *Tectonophysics* **125,** 1–16.

Kim, K.-H., J.-M. Chiu, J. Pujol, and K.-C. Chen (2006). Polarity reversal of active plate boundary and elevated oceanic upper mantle beneath the collision suture in Central Eastern Taiwan, *Bull. Seismol. Soc. Am.* **96,** no. 3, 796–806.

Kim, K.-H., J.-M. Chiu, J. Pujol, K.-C. Chen, B.-S. Huang, Y.-H. Yeh, and P. Shen (2005). Three-dimensional V_P and V_S structural models associated with the active subduction and collision tectonics in Taiwan region, *Geophys. J. Int.* **162,** no. 1, 204–220, doi: 10.1111/j.1365-246X.2005.02657.x.

Kirkpatrick, S., C. D. Gelatt, and M. P. Vecchi (1983). Optimization by simulated annealing, *Science, New Series* **220,** no. 4598, 671–680.

Lee, J.-C., and J. Angelier (1993). Location of active deformation and geodetic data analyses: an example of the Longitudinal Valley Fault, Taiwan, *Bulletin de la Société Géologique de France* **164,** 533–570.

Lee, J.-C., J. Angelier, H.-T. Chu, S.-B. Yu, and J.-C. Hu (1998). Plate-boundary strain partitioning along the sinistral collision suture of the Philippine and Eurasian plates: Analysis of geodetic data and geological observation in southeastern Taiwan, *Tectonics* **17,** no. 6, 859–871.

Li, Z.-W., Y. Xu, T.-Y. Hao, and Y. Xu (2009). V_P and V_P/V_S structures in the crust and upper mantle of the Taiwan region, China, *Sci. China Earth Sci.* **52,** no. 7, 975–983, doi: 10.1007/s11430-009-0091-2.

Mozziconacci, L., B. Delouis, J. Angelier, J.-C. Hu, and B.-S. Huang (2009). Slip distribution on a thrust fault at a plate boundary: The 2003 Chengkung earthquake, Taiwan, *Geophys. J. Int.* **177,** no. 2, 609–623, doi: 10.1111/j.1365-246X.2009.04097.x.

Nabelek, J. L. (1984). Determination of earthquake source parameters from inversion of body waves, *Ph.D. Thesis*, Mass. Inst. of Technol., Cambridge.

Olson, A. H., and R. J. Aspel (1982). Finite fault and inverse theory with applications to the 1979 Imperial Valley earthquake, *Bull. Seismol. Soc. Am.* **72,** 1969–2001.

Page, B. M., and J. Suppe (1981). The Pliocene Lichi melange of Taiwan; its plate-tectonic and olistostromal origin, *Am. J. Sci.* **281,** 193–227.

Peyret, M., S. Dominguez, R. Cattin, J. Champenois, M. Leroy, and A. Zajac (2011). Present-day interseismic surface deformation along Longitudinal Valley, eastern Taiwan, from PS-InSAR analysis of the ERS satellite archives, *J. Geophys. Res.* **112,** 21 pp., B03402.

Rau, R.-J., and F.-T. Wu (1995). Tomographic imaging of lithospheric structures under Taiwan, *Earth Planet. Sci. Lett.* **133,** 517–532.

Savage, J. C. (1980). Dislocations in seismology, in *Dislocations in Solids*, F. R. N. Navarro (Editor), North-Holland, Amsterdam.

Seeber, L., J. G. Armbruster, N. Ozer, M. T. Aktar, S. Baris, D. Okaya, Y. Ben-Zion, and N. Field (2000). The 1999 earthquake sequence along the North Anatolian Transform at the junction between two main ruptures, in *The 1999 Izmit and Dzce Earthquakes; Preliminary results*, A. Barka, O. Kozaci, S. Akuz, and E. Altunel (Editors), Technical University, Istanbul, Istanbul, 209–333.

Shyu, J. B. H., K. Sieh, Y.-G. Chen, and L.-H. Chung (2006). Geomorphic analysis of the Central Range fault, the second major active structure of the Longitudinal Valley suture, eastern Taiwan, *Geol. Soc. Am. Bull.* **118,** nos. 11–12, 1447–1462, doi: 10.1130/B25905.1.

Shyu, J. B. H., K. Sieh, Y.-G. Chen, Y.-R. Chuang, Y. Wang, and L.-H. Chung (2008). Geomorphology of the southernmost Longitudinal Valley fault: Implications for evolution of the active suture of eastern Taiwan, *Tectonics* **27,** 22, TC1019, doi: 10.1029/2006TC002060.

Teng, T.-L., W.-S. Chen, Y. Wang, S.-R. Song, and H.-J. Lo (1988). Toward a comprehensive stratigraphic system of the Coastal Range, eastern Taiwan, *Acta Geologica Taiwanica* **26,** 19–36.

Tsai, Y. B. (1986). Seismotectonics of Taiwan, *Tectonophysics* **125,** 17–31.

Tsai, Y. B., Y. M. Hsiung, H. Liaw, H. P. Lueng, H. P. Yao, Y. H. Yeh, and Y. T. Yeh (1974). A seismic refraction study of eastern Taiwan, *Petrol. Geol. Taiwan* **11,** 165–182.

Wells, D. L., and K. J. Coppersmith (1994). New empirical relationships among magnitude, rupture length, rupture width, rupture area, and surface displacement, *Bull. Seismol. Soc. Am.* **84,** no. 4, 974–1002.

Wu, Y.-M., C.-H. Chang, L. Zhao, J. B. H. Shyu, Y.-G. Chen, K. Sieh, and J.-P. Avouac (2007). Seismic tomography of Taiwan: Improved constraints from a dense network of strong motion stations, *J. Geophys. Res.* **112,** 13, B08312, doi: 10.1029/2007JB004983.

Wu, Y.-M., Y.-G. Chen, C.-H. Chang, L.-H. Chung, T.-L. Teng, F.-T. Wu, and C.-F. Wu (2006). Seismogenic structure in a tectonic structure zone: With new constraints from 2006 M_w 6.1 Taitung earthquake, *Geophys. Res. Lett.* **33,** 5, L22305, doi: 10.1029/2006GL027572.

Yeh, E.-C., D. M. Fisher, S. D. Willett, and S. L. Greenan (2001). Structure, kinematics, and thermal/erosion history of the eastern Central Range,

Taiwan, Presented at *American Geophysical Union, Fall Meeting 2001*, Abstract #T32A-0875.

Yü, M.-S. (1996). Present and recent kinematics of the Pinanshan Conglomerate, eastern Taiwan, Presented at *Annual Meeting of Geological Society of China*, Taipei.

Yu, S.-B., and L.-C. Kuo (2001). Present-day crustal motion along the Longitudinal Valley Fault, eastern Taiwan, *Tectonophysics* **333,** 199–217.

Yu, S.-B., D. D. Jackson, G.-K. Yu, and C.-C. Liu (1990). Dislocation model for crustal deformation in the Longitudinal Valley area, eastern Taiwan, *Tectonophysics* **183,** 97–109.

Yu, T.-C., and S.-H. Hung (2012). Temporal changes of seismic velocity associated with the 2006 M_w 6.1 Taitung earthquake in an arc-continent collision suture zone, *Geophys. Res. Lett.* **39,** 7, L12307, doi: 10.1029/2012GL051970.

Institute of Earth Sciences
Academia Sinica
128, Sec. 2, Academia Road
Nangang, Taipei 11529, Taiwan
laetitia@earth.sinica.edu.tw
(L.M., B.-S.H., J.-C.L.)

Géoazur
250 rue Albert Einstein Les Lucioles 1
Sophia Antipolis 06560 Valbonne, France
(B.D., N.B.)

Manuscript received 24 August 2011